

# Spectroscopy and Linear Spectropolarimetry of the early Herbig Be Stars PDS 27 and PDS 37<sup>\*</sup>

K. M. Ababakr<sup>1†</sup>, J. R. Fairlamb<sup>1</sup>, R. D. Oudmaijer<sup>1</sup> and M.E. van den Ancker<sup>2</sup>

<sup>1</sup>*School of Physics and Astronomy, University of Leeds, EC Stoner Building, Leeds LS2 9JT, UK*

<sup>2</sup>*European Southern Observatory, Karl-Schwarzschild-Str.2, D-85748 Garching bei München, Germany*

Accepted 2015 July 2. Received 2015 July 1; in original form 2014 September 29

## ABSTRACT

The number of well-studied early-type pre-main-sequence objects is very limited, hampering the study of massive star formation from an observational point of view. Here, we present the results of VLT/FORS2 spectropolarimetric and VLT/X-shooter spectroscopic observations of two recently recognised candidate Herbig Be stars, PDS 27 and PDS 37. Through analysis of spectral lines and photometry, we find that these two objects are hot,  $17500 \pm 3500$  K, have large radii,  $17.0 \pm 4.0$  and  $25.8 \pm 5.0$   $R_{\odot}$ , and are very massive,  $15.3 (+5.4, -4.4)$  and  $21.1 (+11.0, -5.3)$   $M_{\odot}$  for PDS 27 and PDS 37, respectively. This suggests that these two objects are very young in their evolution and may become O-type stars. Their youth is supported by their high accretion rates of the order of  $10^{-3}$ – $10^{-4.5}$   $M_{\odot}/\text{yr}$ . A change in linear polarisation across the absorption component of  $H\alpha$  is detected in both objects. This change indicates that the circumstellar environment close to the star, at scales of several stellar radii, has a flattened structure, which we identify as an inner accretion disc. Strong variability is seen in both objects in many lines as further indication of an active circumstellar environment.

**Key words:** techniques: polarimetric – techniques: spectroscopic – circumstellar matter – stars: pre-main-sequence – individual: PDS 27 – individual: PDS 37.

## 1 INTRODUCTION

Herbig Ae/Be (HAeBe) stars are optically visible pre-main-sequence (PMS) stars with masses roughly between 2 and 10  $M_{\odot}$ . With their intermediate masses, they bridge the gap between low-mass stars whose formation is well understood and high-mass stars whose formation is poorly understood (Zinnecker & Yorke 2007). HAeBe objects were first identified by Herbig (1960) as stars of spectral type A or B with emission lines and which illuminate a bright nebula in their surroundings. Their spectral energy distributions (SEDs) are characterised by an infrared excess due to the dust in the circumstellar environment (Waters & Waelkens 1998).

HAeBe objects not only have some common characteristics with high-mass objects such as clustering (Testi et al. 1999) but also have spectropolarimetric characteristics in common with T Tauri stars (Vink et al. 2002). Therefore, the study of the formation of HAeBe stars can bring out the

differences in the mechanisms of the formation of low- and high-mass stars. In addition, because they are closer and less embedded than massive young stars, HAeBe stars can act as a powerful test bed for the formation of massive stars.

To study the star formation mechanism as a function of mass, it is necessary to sample a large number of HAeBe stars, with many representatives in all mass bins. The known sample of HAeBe stars [see e.g. the catalogue by The et al. (1994)] contains many A-type and late B-type objects, but there is a dearth of the earliest type, most massive Herbig Be (HBe) stars (also see e.g. Ochsendorf et al. (2011)). In this paper we present an in-depth investigation of two early HBe star candidates identified by the Pico dos Dias Survey (PDS). Based on their observational characteristics, PDS 27 (also known as DW CMa, RA 07:19:36, Dec.  $-17:39:18$ ) and PDS 37 (also known as Hen 3-373, RA 10:10:00, Dec.  $-57:02:07.3$ ) were proposed to be early type Herbig stars by Vieira et al. (2003). The young nature of PDS 27 was also suggested by Suárez et al. (2006). Both stars were also classified as young in the Red MSX Source (RMS) survey for Massive Young Stellar Objects (MYSOs) (Lumsden et al. 2013). In 2011, Vieira et al. (2011) considered PDS 27 to be an evolved star instead, but ruled out an evolved nature

<sup>\*</sup> Based on observations collected at the European Southern Observatory (ESO), Paranal, Chile under programme ID 084.C-0952(A), 088.C-0858(A), 088.C-0858(B) and 088.C-0858(C).

<sup>†</sup> E-mail: pykma@leeds.ac.uk

for PDS 37. However, as we will demonstrate in this paper, both objects are very similar, and we proceed under the assumption that they are young stars.

Using optical photometry, the temperature has been estimated to be around 22000 K for both objects (Vieira et al. 2003). Vieira et al. (2003) also estimated their distance and it was found to be 1100 pc for PDS 27 and 720 pc for PDS 37; PDS 27 is associated with CMa star-forming region while PDS 37 is associated with C 282.4+0. Ilee et al. (2013) studied the near-infrared (NIR) first overtone CO emission of PDS 37, and assuming that it originates from the circumstellar disc, they found the disc to be highly inclined to the line of sight ( $80^\circ$ ). Rodrigues et al. (2009) determined an intrinsic polarisation of 2.77% for PDS 37, suggesting that the circumstellar environment is not spherical.

Here we present a spectroscopic and spectropolarimetric study of these two objects. We will use the large wavelength coverage provided by X-shooter to determine the stellar parameters, evolutionary status and accretion rates. Spectropolarimetry is a very powerful technique that can probe very small unresolved spatial scales of the order of stellar radii and allows one to extract information on the geometry of this material (see e.g. Oudmaijer & Drew (1999); Vink et al. (2002, 2005)). A new element in the present study is that the medium-resolution spectropolarimetry has a wavelength coverage from 4560 to 9480 Å, which is much larger than presented in any previous study at similar spectral resolution.

This paper is organised as follows: in Section 2 the observations and data reduction are discussed. The results are presented in Section 3. Section 4 presents an analysis of the data followed by a discussion in Section 5. Finally, conclusions are drawn in Section 6.

## 2 OBSERVATIONS

### 2.1 Spectropolarimetry

The data of PDS 27 and PDS 37 were taken as part of a wider spectropolarimetric investigation whose results will be presented in a future paper (Ababakr et al., in preparation). The targets were selected based on their strong emission lines, allowing an investigation into their spectropolarimetric behaviour.

The spectropolarimetric data for our targets were obtained during the nights of 2012 February 4 and 5 with the FORS2 spectrograph mounted on ESO's VLT in Chile. Three gratings were used with a  $4096 \times 2048$  pixel CCD to sample the entire optical range. The 1400V grating with central wavelength 5200 Å covered the spectral range from 4560 to 5860 Å and includes H $\beta$ . The 1200R grating was used for the spectral range from 5750 to 7310 Å, with central wavelength 6500 Å, and includes notable lines: H $\alpha$ , [O I] 6300 Å, and He I lines at 5875, 6678 and 7065 Å. Finally, the 1027Z grating covers 7730 – 9480 Å, at central wavelength 8600 Å, and this includes the calcium triplet lines and the hydrogen Paschen series. A 0.5 arcsec slit was used in all cases, which resulted in a spectral resolution of  $R = 3800, 4800, 4800$  in the V, R and Z bands respectively.

FORS2 is equipped with an optical polarimeter in order to analyse the linearly polarised components. The polarisation optics consist of a rotating half-wave plate and a

calcite block. The calcite block separates the incoming light into two perpendicularly polarised light beams, the ordinary (O) and extraordinary (E) beam. The half-wave plate is rotated to measure polarisation at four different angles:  $0^\circ$ ,  $45^\circ$ ,  $22.5^\circ$ , and  $67.5^\circ$ . One complete set of observations consists of four exposures, one at each of the four angles. To avoid saturation in the bright emission lines, several sets of observations were taken with short exposure times.

The polarisation accuracy is determined only by photon statistics; in order to reach a relative accuracy of 0.1%, one needs to detect roughly one million photons per resolution element. The targets are relatively faint, with V-band magnitudes of 13.0 and 13.5 for PDS 27 and PDS 37 respectively (Vieira et al. 2003), so the total integration times were comparatively long with 1.6 and 2.4h total. For PDS 27 the exposure times are broken down into  $8 \times 340$ s for the V-grating,  $24 \times 50$ s for the R-grating and  $16 \times 120$ s for the Z-grating. Similarly for PDS 37 the times are  $16 \times 340$ s for the V-grating,  $24 \times 70$ s for the R-grating and  $16 \times 100$ s for the Z-grating. Polarised and unpolarised standard stars were observed throughout the night. The exposure times for these were much shorter as it was only the continuum values that were of interest.

The spectropolarimetric data reduction was carried out using GASGANO and FORS pipeline v4.9.18. We have used two recipes: one dedicated to the calibration and the other to extract the science spectrum. The reduction procedure consists of bias subtraction, flat fielding, extraction and wavelength calibration of the O and E spectra. The Stokes parameters, obtained from the O and E beams, lead to the percentage of linear polarisation,  $P$ , and polarisation angle,  $\theta$ , according to the following equations:

$$P = \sqrt{Q^2 + U^2} \quad (1)$$

$$\theta = \frac{1}{2} \arctan \left( \frac{U}{Q} \right) \quad (2)$$

Finally, the spectropolarimetric data were imported into the IRAF and POLMAP package for measurement and analysis.

FORS2 is mounted on the UT1 Cassegrain focus, resulting in a relatively stable instrumental polarisation. To improve signal-to-noise and the polarisation accuracy, the individual data sets were combined. The instrumental polarisation is determined from the observation of unpolarised standard stars. This was found to be  $\sim 0.16\%$ . The polarisation angle has an absolute error of  $\sim 0.5^\circ$  as determined from observing polarised standard stars. We did not perform a correction for instrumental polarisation as it is small compared to the continuum values of the targets, while our main emphasis lies on the differential polarisation between lines and continuum.

### 2.2 Spectroscopy

Spectra of PDS 27 and PDS 37 were obtained using the medium-resolution spectrograph X-shooter, mounted on the VLT, Chile (Vernet et al. 2011) as part of a larger programme (Oudmaijer et al. 2011; Fairlamb et al. 2015). One of the main strengths of the instrument is its huge wavelength coverage, taken simultaneously, over three arms: 3000 – 5900Å, UVB; 5300Å – 1.0 $\mu$ m, VIS; and 1.0 – 2.4 $\mu$ m, NIR.

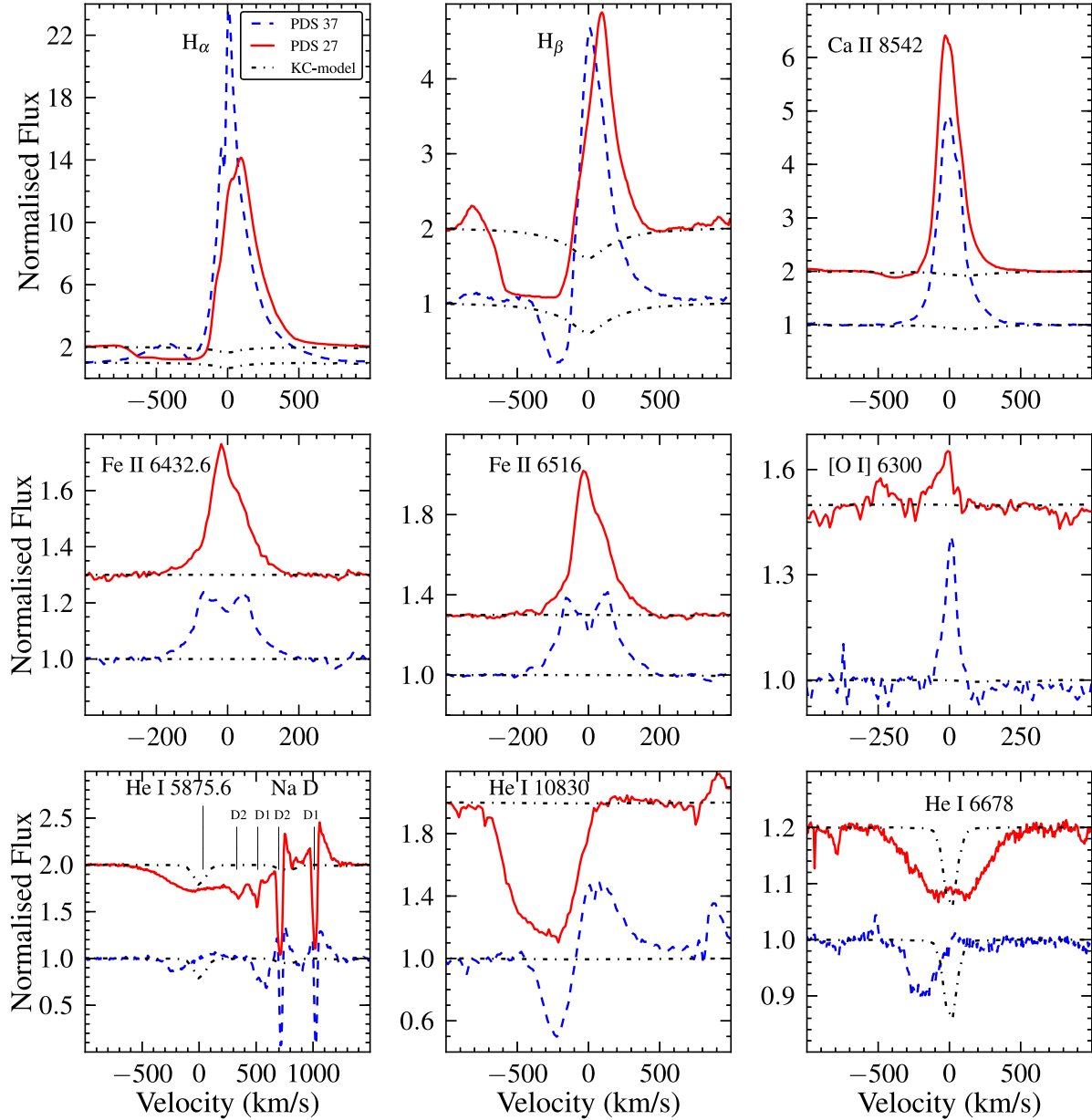


**Figure 1.** A selection of observed spectral lines from the X-shooter data is shown for both targets (for PDS 27 only the X-shooter(b) data set is shown for clarity). The spectra are shifted such that their systemic velocity (see the text) is  $0 \text{ km s}^{-1}$ . The red solid line denotes PDS 27, while the blue dashed line is PDS 37. The black dash-dotted line is a Kurucz-Castelli (KC) model atmosphere for a 21000 K type star (Kurucz 1993; Castelli & Kurucz 2004); this is an upper limit to the temperature (this limit will be discussed in Section 4.1.3). The spectra of both objects are normalised to one but PDS 27 is shifted by an arbitrary value for clarity. Note the similarity of both objects' spectra, with a difference being the number of double-peaked lines of Fe II in PDS 37. Blueshifted absorption reaching  $-700$  and  $-400 \text{ km s}^{-1}$  is observed in  $H\alpha$  and helium for PDS 27 and PDS 37, respectively.

The smallest slit widths available (0.5 arcsec - UVB, 0.4 arcsec - VIS and 0.4 arcsec - NIR) were used and provided the highest spectral resolution available for X-shooter:  $R=9100$ , 17400 and 11300, respectively. Both objects were observed in nodding mode in an ABBA sequence. Two observations were made of PDS 27, on the evenings of 2009 December 18 and 2010 February 24 (these data sets will be referred to as X-shooter(a) and X-shooter(b), respectively, for the remainder of this paper). The exposures were the same for each observation with a breakdown across the arms of UVB

- 300s $\times$ 4, VIS - 300s $\times$ 4 and NIR - (2s $\times$ 6) $\times$ 4. PDS 37 was observed on the evening of 2010 March 31 with exposures of UVB - 300s $\times$ 4, VIS 300s $\times$ 4, and NIR (3s $\times$ 6) $\times$ 4. The spectra of both objects were reduced using the X-shooter pipeline v0.9.7 (Modigliani et al. 2010) following standard reduction procedures (flat-fields, wavelength calibration, etc.). The final wavelength calibration was carried out manually by identifying several telluric absorption lines using a solar spectrum catalogue (Delbouille et al. 1973).

The UVB is corrected for instrumental response across

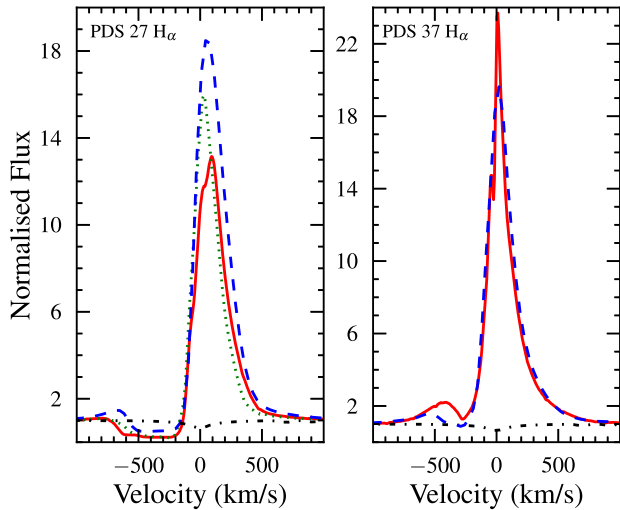


**Figure 2.**  $H\alpha$  line variability from three observation epochs for PDS 27: FORS2 (blue dashed line) and two X-Shooter epochs, X-shooter(a) (green dotted line) and X-shooter(b) (red solid line). For PDS 37, there is only one X-shooter data set (red solid line). A KC model (black dash-dotted line) of temperature 21000 K is also overplotted. The lines are shifted to the rest wavelength of the stars as in Fig. 1.

the Balmer jump region (in order to measure the Balmer excess, which is a diagnostic for the strength of the accretion). To do this the observed spectra of the flux standards were divided through by the known flux from CALSPEC<sup>1</sup>. The resulting response curve was then applied to the target of that night. To measure the Balmer excess, we do not need an absolute flux calibration, only the correct shape of the SED is needed. This method of calibration is therefore sufficient. We require only knowledge of the line strengths, profile shapes and calibrated wavelengths in the other arms. Therefore, this calibration is not needed in the other arms.

### 3 RESULTS

#### 3.1 Spectral lines

The spectra of both stars are remarkably similar showing numerous emission lines, while there is a paucity of photospheric absorption lines. A representative set of lines is shown in Fig. 1.

The strongest emission is found among the hydrogen recombination lines, Fe II, Ca II and [O I]. The  $H\alpha$  and  $H\beta$  lines have P Cygni profiles, with absorption observed at velocities in excess of 500  $\text{km s}^{-1}$  in the case of PDS 27, with some emission observed bluewards of the P Cygni absorption. The  $H\alpha$  lines are very strong with line-to-continuum ratios of the order of 20 and an equivalent width (EW) of -70.4 and -111.4  $\text{\AA}$  for PDS 27 and PDS 37, respectively. Several strong Fe II emission lines can be seen in the visible portion of the spectra; the majority of these are double peaked in PDS 37, while they are all single peaked in PDS 27. Strong emission is also present in the Ca II triplet (8498, 8542,

8662  $\text{\AA}$ ) and Ca II doublet (8912, 8927  $\text{\AA}$ ) in both stars. The Ca II triplet lines are blended with the Paschen lines at 8502, 8545 and 8665  $\text{\AA}$ . The Ca II line at 8542 and 8662  $\text{\AA}$  in PDS 27 has a very weak blueshifted absorption. The other nearby Paschen lines at 8598, 8750 and 8863  $\text{\AA}$  have similar absorption components. Therefore, the absorption seen in the Ca II lines is more likely to belong to the Paschen series with which they are blended. He I lines at 5875, 6678, 7065 and 10830  $\text{\AA}$  are in absorption and blueshifted to the same velocities as observed in the hydrogen P Cygni profiles. He I at 10830  $\text{\AA}$  has a P Cygni profile in PDS 37 with absorption observed up to -450  $\text{km s}^{-1}$ , and the EW of the emission is slightly larger than that of the absorption. For PDS 27, He I at 10830  $\text{\AA}$  has a very strong absorption up to -700  $\text{km s}^{-1}$  and is accompanied by a very weak redshifted emission component. As we go from low-order lines in the hydrogen Balmer series ( $H\alpha$ ,  $H\beta$ ) towards the higher order hydrogen lines, we see a progressively weaker absorption component in each line. The only exception is that the absorption in  $H\alpha$  is less deep than in  $H\beta$ , which we shall discuss later. The varying hydrogen line profiles prevent a reliable measurement of the stars' radial velocity ( $V_r$ ). Therefore, to obtain the systemic velocity, we measure the  $V_r$  from the clean and symmetric Fe II and Ca II triplet lines in the X-shooter and FORS2 spectra. The measured  $V_r$  are corrected for heliocentric motion and local standard of rest motion for the dates of observation. These give local standard of rest velocities ( $V_{\text{LSR}}$ ) of  $47.2 \pm 3.4$ ,  $45.3 \pm 4.3$ , and  $63 \pm 7 \text{ km s}^{-1}$  for PDS 27 X-shooter(a), X-shooter(b) and FORS2, respectively. Both X-shooter(a) and X-shooter(b) values are in agreement with each other, while there is a difference of  $\sim 18 \pm 8 \text{ km s}^{-1}$  between X-shooter and FORS2. For PDS 37, the  $V_{\text{LSR}}$  is found to be  $11.7 \pm 5.5 \text{ km s}^{-1}$  for X-shooter and  $13.5 \pm 8.0 \text{ km s}^{-1}$  for FORS2. For the final  $V_{\text{LSR}}$  to PDS 37 an average of the X-shooter and FORS2 values is taken and this results in a  $V_{\text{LSR}}$  of  $12.6 \pm 4.8 \text{ km s}^{-1}$ .

Both stars' spectra are variable. An illustration of this is provided in Fig. 2 in which we show  $H\alpha$  at three observation epochs for PDS 27 and two for PDS 37. The line profiles are variable with a deeper absorption component when the emission is weaker. For PDS 27 the  $H\alpha$  line-to-continuum ratio ranges from 13 to 18, and the EW increases from -70.4 to -120.8  $\text{\AA}$  from the X-shooter(b) to the FORS2 data sets (with the X-shooter(a) observations lying in between). For PDS 37 the line-to-continuum increases from 19.5 to 24, and the EW from -111.4 to -122.6  $\text{\AA}$ . Vieira et al. (2011) observed, in 1990, an EW of -88 and -105  $\text{\AA}$  for PDS 27 and PDS 37 respectively.

Variability of the He I line in PDS 27 also occurs between all observations. Fig. 3 shows four of the He I lines, along with overplots from each observation epoch in order to highlight the variability. The He I lines 5875, 6678 and 7065  $\text{\AA}$  are present in both X-shooter and FORS2 spectra, while 10830  $\text{\AA}$  is covered only by the X-shooter observations. The 5875  $\text{\AA}$  line in the FORS2 data shows a broad blue absorption wing which is seen extending from -500  $\text{km s}^{-1}$  towards the red, but we cannot quantify how far it extends into the red due to the Na I lines blending with it. In the X-shooter(a) data set a clear absorption line is seen centred at  $\sim -150 \text{ km s}^{-1}$  from the rest wavelength. The line in the X-shooter(b) is difficult to measure, due to the blending mentioned, but it appears to be centred at  $\sim -100 \text{ km s}^{-1}$ .

<sup>1</sup> <http://www.stsci.edu/hst/observatory/crds/calspec.html>



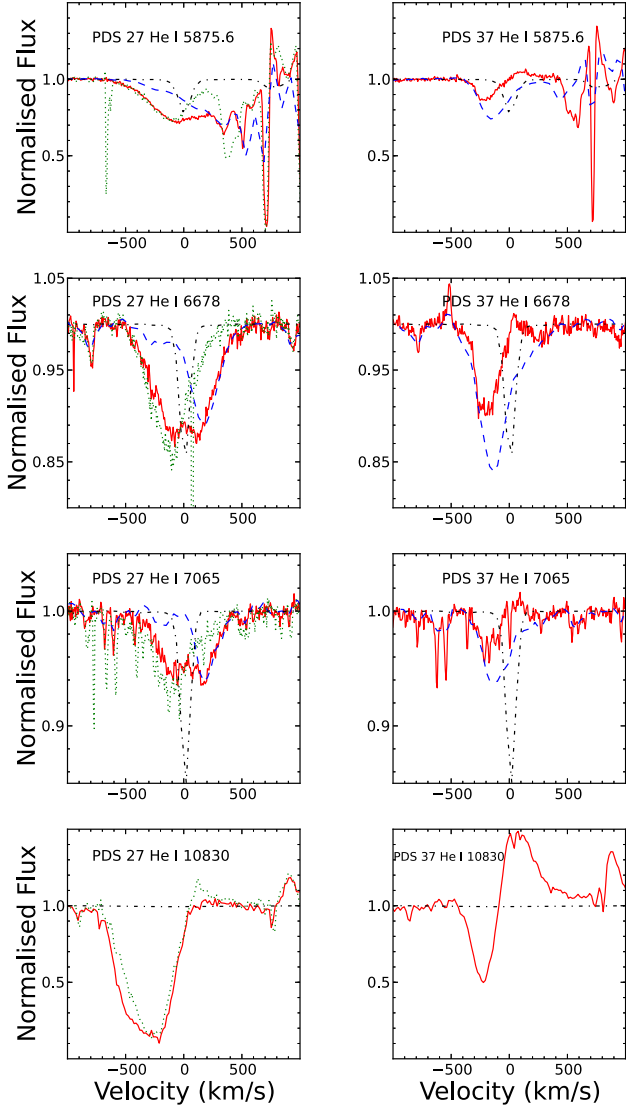


**Figure 3.** He I line variability is shown for PDS 27 of three observation epochs: FORS2 (blue dashed line) and two X-shooter epochs, X-shooter(a) (green dotted line) and X-shooter(b) (red solid line). For PDS 37, there is only one X-shooter data set (red solid line) and one FORS2 observation (blue dashed line). A KC model (black dash-dotted line) of temperature 21000 K is overplotted for the 5875, 6678 and 7065 Å lines, while for the 10830 Å line a black dash-dotted line shows just the continuum level. The lines are shifted to the rest wavelength of the stars as in Fig. 1.

The 6678 and 7065 Å lines show a similar behaviour in their velocities between the data sets, as demonstrated in Fig. 3. The 10830 Å line only shows a small variability in the strength of the line.

In the case of PDS 37, all the He I lines, present in both X-shooter and FORS2, show variability in the line centre of  $\sim 50 \text{ km s}^{-1}$  between them, with respective line centres being blueshifted from the central wavelength. Some of these show a very weak redshifted emission, which is seen to be much stronger in the 10830 Å line. There is also strong variability in the line strengths, measured solely across the absorption component, where the strength is  $\sim 2.5$  greater in FORS2 than in X-shooter.

**Table 1.** The observed EW and the  $E(B-V)$  values obtained from the DIBs. Errors in the EW and  $E(B-V)$  are typically 5%.

DIB (Å)	EW/ $E(B-V)$ (mÅ/mag.)	PDS 27		PDS 37	
		EW (mÅ)	$E(B-V)$ (mag)	EW (mÅ)	$E(B-V)$ (mag)
5780.6	579	571.5	0.99	278.9	0.48
5797.1	132	190.7	1.44	221.6	1.68
5849.8	48	116.4	2.42	139.4	2.90
6089.8	17	24.1	1.42	23.4	1.38
6204.3	189	230.8	1.22	129.0	0.68
6013.7	23	242.0	1.05	206.5	0.89
6660.6	51	61.8	1.21	46.9	0.90
6993.2	116	131.7	1.06	100.0	0.86

### 3.2 Interstellar lines

The spectra of both targets contain interstellar absorption lines, most notably the K I doublet (7664.9, 7698.9 Å), Na I doublet (5889.9, 5895.9 Å) and the diffuse interstellar bands (DIBs); their origin comes from the material present in the interstellar medium (ISM). The strength of the DIBs increases with the amount of material, and therefore reddening, along the line of sight (Jenniskens & Desert 1994). However, the DIBs can only provide a lower limit to the total reddening. Oudmaijer et al. (1997) found for a sample of young objects that the majority of the DIBs correlate with the reddening due to interstellar dust, but they remain insensitive to the dust in circumstellar envelopes and their parental molecular clouds. Eight well-known DIBs are clearly identified in both objects; the measured EW for each line, along with the line strength per unit  $E(B-V)$  determined from Jenniskens & Desert (1994), and the resulting  $E(B-V)$  are given in Table 1. The overall  $E(B-V)$  is found to be  $1.2 \pm 0.16$  for PDS 27 and  $0.98 \pm 0.37$  for PDS 37. The spread of the values is fairly large with  $E(B-V)$  ranging, for PDS 27 and 37 respectively, from a low of 0.99 and 0.48, for the 5780 Å line, to a high of 2.42 and 2.9, for the 5849 Å line. The very large colour excess derived from the 5849 Å DIB is not entirely unexpected as it was suggested by Chlewicki et al. (1986) that the strength of this DIB could provide a good indication of the total reddening towards an object including the circumstellar component. This argument is strengthened by Oudmaijer et al. (1997) who found in their study that this DIB was an exceptionally case which more accurately traced the total reddening for each star than any of the other DIBs. Therefore, in the overall  $E(B-V)$  reported above, the 5849 Å DIB is not included. The  $V_{\text{LSR}}$  of the DIBs is measured to be  $26.6 \pm 5.3$ ,  $27.3 \pm 5.6$  and  $27.5 \pm 2 \text{ km s}^{-1}$  for PDS 27 X-shooter(a), X-shooter(b) and FORS2 spectra, respectively; all the values are in very good agreement with each other. For PDS 37, the  $V_{\text{LSR}}$  is found to be  $0.5 \pm 2.8$  and  $6 \pm 4 \text{ km s}^{-1}$  for the X-shooter and FORS2 spectra, respectively. This is consistent with the  $V_{\text{LSR}}$  observed in the sharp absorption lines from Na I 5889.9 and 5895.9 Å, which is found to be  $26.5 \pm 1$ ,  $26.8 \pm 0.3$  and  $26 \pm 2 \text{ km s}^{-1}$  for PDS 27 X-shooter(a), X-shooter(b) and FORS2 spectra, respectively, and  $-4.5 \pm 0.5$  and  $-5 \pm 1$  for PDS 37 X-shooter and FORS2 spectra, respectively.

**Table 2.** The continuum polarisation of both objects measured in the following wavelength regions: *B* band centred at 4700 Å, *V* band centred at 5500 Å, *R* band centred at 7000 Å, *I* band centred at 9000 Å. The polarisation was measured over a wavelength range of 250 Å either side of the central wavelength, except for the *B* band where it was 125 Å either side. All the errors are differential, where the systematic error is  $\sim 0.16\%$  in polarisation and  $\sim 0.5^\circ$  in angle (see the text in Section 2.1 for details).

Object	<i>B</i>		<i>V</i>		<i>R</i>		<i>I</i>	
	$P_{cont}(\%)$	$\theta_{cont}^\circ$	$P_{cont}(\%)$	$\theta_{cont}^\circ$	$P_{cont}(\%)$	$\theta_{cont}^\circ$	$P_{cont}(\%)$	$\theta_{cont}^\circ$
PDS 27	$8.60 \pm 0.03$	$18.64 \pm 0.11$	$9.00 \pm 0.01$	$18.87 \pm 0.01$	$8.83 \pm 0.01$	$18.36 \pm 0.04$	$7.49 \pm 0.01$	$18.12 \pm 0.03$
PDS 37	$4.68 \pm 0.04$	$129.97 \pm 0.27$	$5.12 \pm 0.01$	$130.80 \pm 0.01$	$5.18 \pm 0.01$	$129.98 \pm 0.06$	$4.38 \pm 0.01$	$133.38 \pm 0.05$

### 3.3 Continuum polarisation

The continuum polarisation of the targets is shown in Fig. 4. In the figure, the spectropolarimetric data were rebinned using a coarse sampling, of  $\sim 250$  Å per bin, to minimize errors. It can be seen that the percentage of polarisation increases from short wavelengths, peaks in the *V* band and then decreases towards longer wavelengths.

The observed continuum polarisation is a combination of interstellar polarisation and polarisation due to circumstellar dust and electron scattering, if the dust and electrons deviate from circular symmetry. The nature of interstellar polarisation is well described and explained by Serkowski et al. (1975). According to Serkowski's law, the linear polarisation follows an empirical curve according to the following equation:

$$\frac{P(\lambda)}{P_{max}} = \exp \left[ -k \ln^2 \left( \frac{\lambda_{max}}{\lambda} \right) \right] \quad (3)$$

where  $\lambda_{max}$  is the wavelength where the polarisation is at its maximum value,  $P_{max}$ , and  $k$  is the width of the empirical curve. Typically,  $\lambda_{max}$  is  $\sim 5500$  Å, but can be in a range of 4500–8000 Å.

The Serkowski law provides an excellent fit to the data and is shown in Fig. 4. This combined with the large  $E(B-V)$  found towards these objects in Section 3.2 suggests that the bulk of the observed polarisation is indeed interstellar. The angle of polarisation changes slightly over the different bands; a change of 1 deg is observed for PDS 27 while a 5 deg change is observed for PDS 37. The polarisation angle normally does not change as a function of wavelength for the ISM. The slight change in position angle with wavelength indicates that there is a contribution from another polarising agent to the total polarisation. The results of continuum polarisation are summarised in Table 2.

### 3.4 Line spectropolarimetry

The polarisation spectra around the strongest lines,  $H\alpha$ ,  $H\beta$  and the calcium triplet are displayed in Fig. 5. There is a clear change in polarisation across the  $H\alpha$  line in both objects. The red peak and, where visible, the blue peak have almost the same polarisation value as the continuum, while there is a strong change across the absorptive component in both polarisation spectra and the  $(Q, U)$  plots. The shift in the polarisation from continuum to the line is of the order of 1% for PDS 27 and 1.6% for PDS 37.

Fig. 5 also shows that there is no clear change in the polarisation spectra across  $H\beta$  for both targets. Several different ways of rebinning the data were tried, but no com-

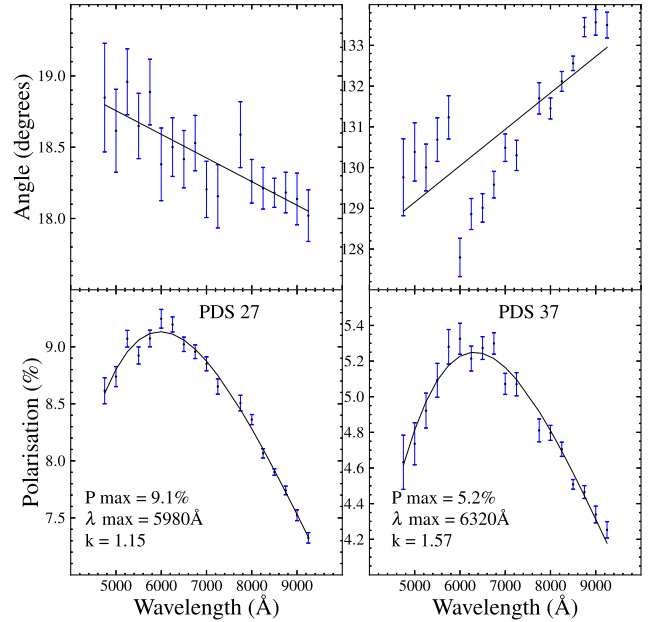


**Figure 4.** The polarisation and polarisation angles as a function of wavelength for PDS 27 and PDS 37. The spectropolarimetric data were coarsely sampled to improve the error bars. The black lines denote the best-fitting Serkowski law to the data.

elling evidence for line effects across  $H\beta$  could be found. Our explanation for this will be discussed in Section 5.1.

The Ca II triplet has a lower ionisation potential than the  $H\alpha$  line, and as such it originates in a different region at a larger distance from the central stars. We did not detect any line effect across the Ca II triplet in PDS 27, whereas in PDS 37, the first two data sets show a possible line effect while the second two data sets do not show such a line effect (see Fig. 5). Therefore, the current data are not sufficient to confirm whether there is a line effect or not across the Ca II triplet in PDS 37. We do not detect changes across any other lines in this polarimetric spectrum, which includes the Ca II doublet, He I, [O I] 6300 Å and Fe II lines.

The observed line characteristics of the targets in the FORS2 data are presented in Table 3, including an indication whether a line effect is present.

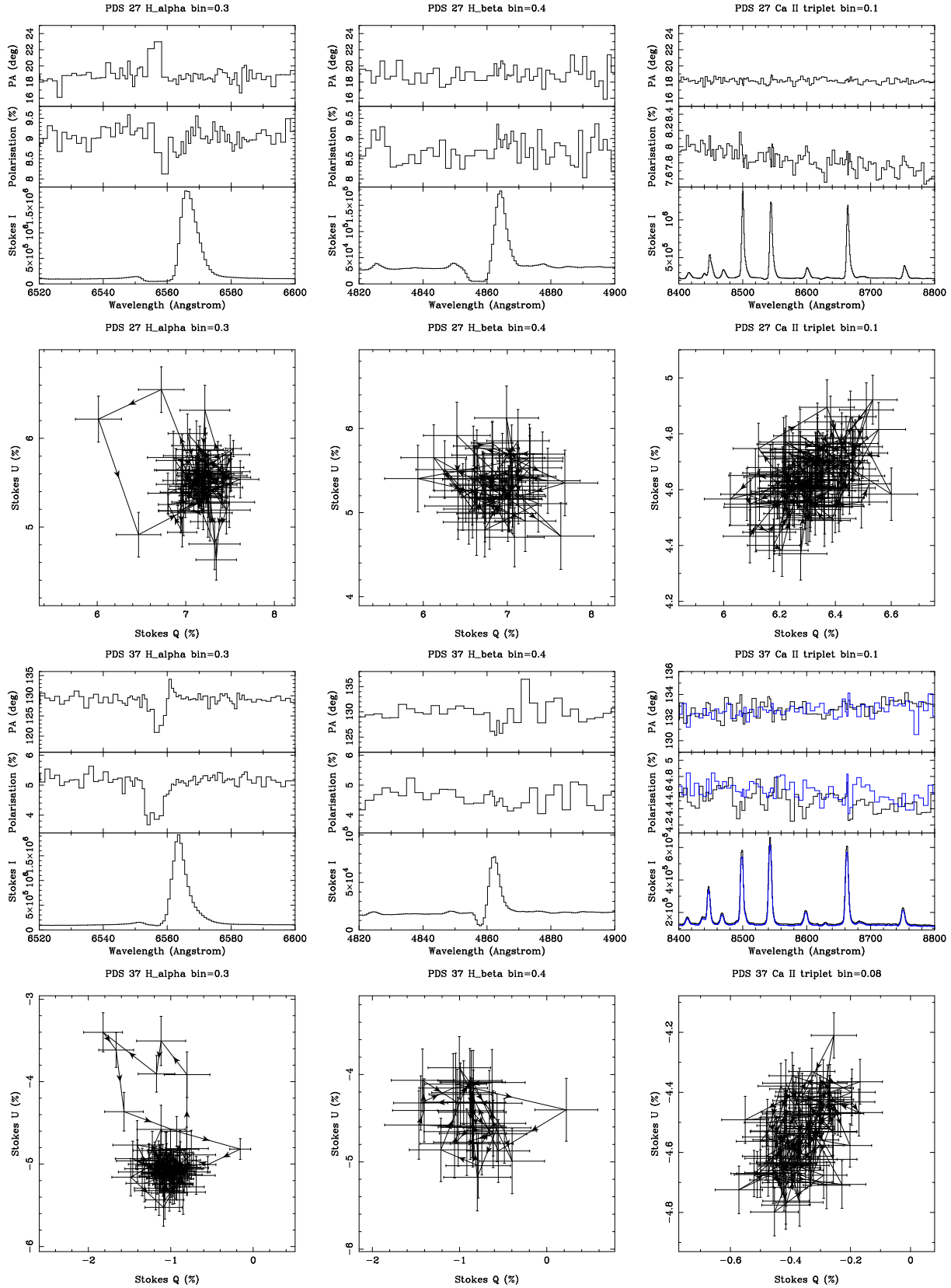


**Figure 5.** The polarisation data of PDS 27 (upper half) and PDS 37 (lower half) are shown here. The data are presented as a combination of triplets (top) and (Q, U) diagrams (bottom). In the triplet polarisation spectra, the Stokes intensity ( $I$ ) is shown in the lowest panel, polarisation (%) in the centre, while the position angle (PA) is shown in the upper panel. The  $Q$  and  $U$  Stokes parameters are plotted against each other below each triplot. The data are rebinned to a constant value, as indicated at the top of each plot. The Ca II triplet in PDS 37 is presented in two colours: the first two data sets with possible line effect are shown in black solid line; the second two data sets with no line effect are shown in blue solid line.

**Table 3.** The line spectropolarimetry results: columns (2), (3), (5) and (6) list the Stokes ( $I$ ) characteristics; columns (4) and (7) list line spectropolarimetry characteristics of each target. Errors in the EW measurements are typically 5%.

Lines	PDS 27			PDS 37		
	EW (Å)	Line/cont.	Line effect	EW (Å)	Line/cont.	Line effect
H $\alpha$	-120.80	18.0	Yes	-122.60	19.4	Yes
H $\beta$	-14.56	5.8	No	-12.27	4.5	No
Ca II(8498)	-24.05	6.0	No	-22.66	4.4	–
Ca II(8542)	-23.97	5.3	No	-25.43	5.1	–
Ca II(8662)	-22.78	5.2	No	-23.12	4.8	–
Ca II(8912)	-1.11	1.2	No	-0.81	1.1	No
Ca II(8927)	-1.79	1.3	No	-1.69	1.3	No
He I(6678)	0.90	0.9	No	1.40	0.8	No
He I(7065)	0.27	0.9	No	0.52	0.9	No
O I(6300)	-0.36	1.1	No	-0.46	1.2	No
Fe II(6456)	-3.14	1.8	No	-2.07	1.5	No

## 4 ANALYSIS

### 4.1 Stellar parameters

#### 4.1.1 Stellar velocity

Due to the lack of photospheric absorption lines in the spectra of both stars, we used the clean and symmetric Fe II and Ca II triplet emission lines to estimate the systemic velocity.

For PDS 27 we noted that in Section 3.1 both X-shooter observations provide a similar  $V_{\text{LSR}}$ , while there is a difference of  $\sim 18 \pm 8 \text{ km s}^{-1}$  in  $V_{\text{LSR}}$  between X-shooter and FORS2. To examine the reliability of this variation, it is important to check the  $V_{\text{LSR}}$  of the interstellar lines as this should not vary over different epochs. In Section 3.2, we found a similar  $V_{\text{LSR}}$  of the DIBs in all epochs. These velocities are consistent with the  $V_{\text{LSR}}$  observed in the sharp absorption lines from Na I 5889.9 and 5895.9 Å. The observed variation in  $V_{\text{LSR}}$  of PDS 27 could be due to the star itself through changes in the circumstellar environment. On the other hand, it could be due to the presence of a second star in the system. Distinguishing conclusively between the two scenarios is challenging with only a few epochs of data, and requires additional observations. However, we found that the line profiles are almost symmetric in all epochs; hence, it is more likely that the changes seen are due to binary motions and are not due to the movements of circumstellar material around the star. Based on the above argument, we decide not to use our stellar velocities for PDS 27 for kinematic distance determinations.

For PDS 37, the  $V_{\text{LSR}}$  is consistent within the errorbars for the X-shooter and FORS2 data.

#### 4.1.2 Distance

Accurate stellar parameters are required for any quantitative analysis to be made about either age, accretion or evolution for these two enigmatic objects. First we will discuss the distance, which will later help constrain the total luminosity.

Using a Galactic rotation curve an estimate of the distance to the stars can be made using the observed velocities. In this work, we use the rotation curve from Reid et al. (2009). The observed  $V_{\text{LSR}}$  in PDS 27 is unlikely to trace the

actual stellar velocity as argued in the previous section. Fortunately, molecular observations of  $^{13}\text{CO}(1-0)$  and  $\text{NH}_3(1,1)$  towards these objects are available (Urquhart et al. 2007, 2011). The molecular lines in this case trace the parental clouds in a larger volume around the star compared to the optical lines. These authors observe velocities of 43.5 and 5.4  $\text{km s}^{-1}$  for PDS 27 and PDS 37, respectively. Using the molecular velocities the resulting kinematic distance for PDS 27 is 3.17 (+0.66, -0.62) kpc, while for PDS 37 the distance is found to be  $3.67 \pm 0.95$  kpc. For PDS 37 the stellar lines can also be used; these provide distances of  $4.53 \pm 0.77$  and 4.74 (+0.75, -0.90) kpc for the lines measured from X-shooter and FORS2, respectively. The molecular and spectral line measurements are in agreement with each other in PDS 37. For the final distance to PDS 37, an average of the three values is taken and this results in a distance of  $4.31 \pm 0.67$  kpc.

An interesting consistency check is to see what the kinematic distances to the DIBs along the line of sight towards the objects are. This is because the DIBs trace the material between us and the star, and should therefore be closer than the stellar and molecular distances. The observed  $V_{\text{LSR}}$  velocities of the DIBs in Section 3.2 provide kinematic distances for PDS 27 of 1.76 (+0.58, -0.55) and 1.80 (+0.58, -0.55) kpc for the X-shooter and FORS2 data, respectively. For PDS 37 the kinematic distances of DIBs are found to be  $2.59 \pm 1.4$  and  $3.76 \pm 0.92$  kpc for the X-shooter and FORS2 data, respectively. These distances are indeed lower than the ones traced by the stellar and molecular lines, which is as expected.

#### 4.1.3 Temperature

Spectral types of both stars are difficult to determine due to a general lack of photospheric absorption lines in the spectra. So far, the only spectral type given to these stars is by Vieira et al. (2003), who assign them both a tentative B2 classification based on their photometry.

A rough lower limit on the temperature can be found using the observed colour indices. Vieira et al. (2003) measure a  $(B - V)_{\text{obs}}$  of 1.32 for PDS 27 and 1.52 for PDS 37. The DIBs provide colour excesses,  $E(B - V)$ , of  $1.20 \pm 0.16$  and  $0.98 \pm 0.37$  for PDS 27 and PDS 37, respectively. Com-



binning the observed and excess colours allows an intrinsic  $(B - V)$  to be derived. This is only a lower limit as the DIBs trace the ISM, but not necessarily the total extinction. The highest  $(B - V)_{int}$  from the DIBs is found to be -0.04 in PDS 27 and 0.15 in PDS 37. This gives a lower limit to the temperatures which corresponds to B9-type star with a temperature of 10000 K and A5-type star with a temperature of 8000 K for PDS 27 and PDS 37, respectively. The stars are likely to be even hotter than this, as this is a lower limit.

An upper limit to the temperature can be placed using the Balmer jump in the spectra. This is because the Balmer jump decreases in size with increasing temperature (for temperatures greater than  $\sim 9000$  K, where the Balmer jump is at its maximum). The observed size of the jump therefore places an upper limit on the photospheric temperature. Moreover, a small jump can also be achieved by cooler stars combined with a flux excess due to accretion. The Balmer jump constraint provides an upper limit of 21000 K. A discussion of the jump and possibility of an excess flux will be given in Section 4.2.1.

The DIBs and Balmer jump constraints give an effective temperature range of 8000 K/10000 - 21000 K. In addition, the observed lines from the two objects suggest that they lie more towards the upper temperature limit.

We detect N I emission lines at 8629 and 8683 Å in both objects. These lines have a high excitation energy ( $\sim 10$  eV), and have only been observed in B-type HAeBe stars, predominately early types (Hamann & Persson 1992). Given that the latest spectral type in which these authors detected both NI emission lines was B6 (corresponding to 14000 K), we infer a revised lower limit to the temperatures of PDS 27 and PDS 37 of around 14000 K.

Based on the above three arguments, which combine knowledge of photometry and spectra, we find the most plausible range to the temperatures to be 14000 - 21000 K. We choose to adopt a temperature of  $17500 \pm 3500$  K for both objects.

In addition, the only absorption lines that are present in both spectra are from He I. If their origin were assumed to be from the photosphere, then their strength would peak at around 21000 K. However, the observed strengths are greater than predicted from stellar model atmospheres, and they are asymmetric. The blueshifted absorption extends all the way to  $-500 \text{ km s}^{-1}$  and covers the same velocity range as the hydrogen lines. Therefore, an additional contribution to the absorption could be due to a strong wind. Although strong absorption has been regularly observed for T Tauri stars in the He I 10830 Å line, such a strong and broad absorption in a wind is not expected in the higher energy transitions of He I in classical T Tauri stars (CTTs) by either theory (Kurosawa et al. 2011) or observations (Beristain et al. 2001). This suggests that the stars are much hotter than CTTs, which is in agreement with the other temperature constraints adopted.

#### 4.1.4 Luminosity

With a limit on both distance and temperature established for the stars, other stellar parameters can now be found. A start will be made with determining the luminosity using the previously observed optical photometry. A total flux needs to be obtained, and due to the limited amount of pho-

tometric observations an extrapolation into the UV must be performed to do this. To assess the UV contribution, Kurucz-Castelli (KC) models are used which provide a surface flux density. The *BVRI* photometry is then dereddened with this law until their shape matches the slope of the KC model for the adopted temperature. The *U* band is excluded due to possible effects of an excess due to accretion, while the longer wavelength photometry is also excluded due to being affected by an IR excess from the dust. To fit the models to the photometry, a scaling factor must be applied, as the models used are in surface flux while the photometry is observed flux. This scaling factor is just a ratio between the distance and radius squared,  $(D/R)^2$ . For a temperature of  $17500 \pm 3500$  K, a respective  $A_V$  and  $D/R$  are found to be  $5.03 \pm 0.13$  and  $186.5 \pm 21.0$  for PDS 27, and  $5.81 \pm 0.13$  and  $167.0 \pm 18.9$  for PDS 37. These reddening values are consistent with the DIB derived values, which were lower limits to the total reddening. Fig. 6 shows the result of dereddening the photometry and a 17500 K KC model fit to the data. The luminosities are then calculated as a sum of the scaled KC model flux multiplied through by the distances found previously. Taking into account the errors on the distance and temperature, the luminosities are calculated to be  $\log(L_*/L_\odot) = 4.39 \pm 0.40$  for PDS 27 and  $\log(L_*/L_\odot) = 4.75 \pm 0.39$  for PDS 37.

#### 4.1.5 Location in the HR diagram

With the luminosity established for each star, along with a well-defined temperature limit, the calculation of remaining stellar parameters through the use of PMS tracks can be performed. In this work, two sets of PMS tracks are adopted: one set by Siess et al. (2000), as they cover up to  $12 M_\odot$ , and the other set from Bernasconi & Maeder (1996), as they cover a larger luminosity and mass range (these are the 15 and  $25 M_\odot$  tracks in Fig. 7). Along each mass track, there is a unique relation between the luminosity and temperature. Fig. 7 shows where PDS 27 and PDS 37 lie on the PMS tracks. Based on their position, we find a mass of  $15.3 (+5.4, -4.4) M_\odot$  for PDS 27 and a mass of  $21.1 (+11.0, -5.3) M_\odot$  for PDS 37. The radius is found straightforwardly from the  $D/R$  values, determined in the previous section, by using the distance. This provides  $17.0 \pm 4.0 R_\odot$  for PDS 27 and  $25.8 \pm 5.0 R_\odot$  for PDS 37. With a mass and radius determined, the  $\log(g)$  is calculated to be  $3.16 \pm 0.27$  for PDS 27 and  $2.94 \pm 0.35$  for PDS 37. The errors in  $\log(g)$  are dominated by the errors in distance. The position of the stars in the HR diagram suggests that they are very young objects, which may be evolving into massive O-type stars.

## 4.2 Accretion rates

Measurement of the accretion rates is done by two separate methods: (1) a direct relationship to the measured Balmer excess and (2) using the strength of accretion-tracing lines.

#### 4.2.1 Accretion rates 1: Balmer excess

The first method of obtaining accretion rates is to measure the Balmer excess,  $\Delta D_B$ . This is defined as the ex-

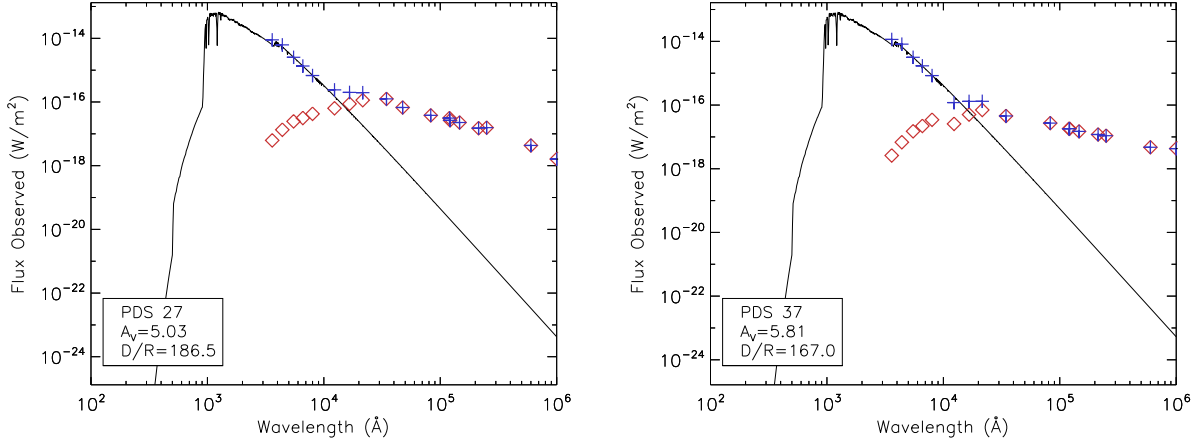


**Figure 6.** An example of the SED integration for extracting a dereddened total flux for the case of PDS 27 (left) and PDS 37 (right). The red diamonds are the observed photometry, the blue crosses are the dereddened photometry and the solid black line is a KC model of 17500 K.

**Table 4.** Lines tracing accretion. Errors in the EW measurements are typically 5%. Errors in the line flux are  $\sim 80\%$ , for both stars, due to the large temperature and distance errors assigned.  $EW_{obs}$ ,  $EW_{int}$  and  $EW_{cor}$  are observed, intrinsic photospheric absorption and corrected EW, respectively.

Line	Star	Spectra	$EW_{obs}$ (Å)	$EW_{int}$ (Å)	$EW_{cor}$ (Å)	$F_{line}$ (W/m <sup>2</sup> )	$\log(L_{line})$ (L <sub>⊙</sub> )	$\log(L_{acc})$ (L <sub>⊙</sub> )	$\log(M_{acc})$ (M <sub>⊙</sub> /yr)
H $\alpha$	PDS 27	X-shooter(a)	-75.20	4.20	-79.40	$1.1 \times 10^{-13}$	$1.54 \pm 0.10$	$3.96 \pm 0.07$	$-3.49 \pm 0.20$
H $\alpha$	PDS 27	X-shooter(b)	-70.40	4.20	-74.60	$1.0 \times 10^{-13}$	$1.52 \pm 0.10$	$3.93 \pm 0.07$	$-3.52 \pm 0.20$
H $\alpha$	PDS 27	FORS2	-120.80	4.20	-125.24	$1.8 \times 10^{-13}$	$1.74 \pm 0.10$	$4.18 \pm 0.06$	$-3.27 \pm 0.19$
[OI] <sub>6300</sub>	PDS 27	X-shooter(a)	-0.28	0.00	-0.28	$4.6 \times 10^{-16}$	$-0.84 \pm 0.10$	$3.85 \pm 0.13$	$-3.60 \pm 0.23$
[OI] <sub>6300</sub>	PDS 27	X-shooter(b)	-0.29	0.00	-0.29	$4.8 \times 10^{-16}$	$-0.82 \pm 0.10$	$3.87 \pm 0.14$	$-3.58 \pm 0.23$
[OI] <sub>6300</sub>	PDS 27	FORS2	-0.36	0.00	-0.36	$5.9 \times 10^{-16}$	$-0.73 \pm 0.10$	$3.97 \pm 0.16$	$-3.48 \pm 0.24$
Br $\gamma$	PDS 27	X-shooter(a)	-3.80	4.72	-4.22	$8.3 \times 10^{-16}$	$-0.58 \pm 0.10$	$3.02 \pm 0.16$	$-4.43 \pm 0.24$
Br $\gamma$	PDS 27	X-shooter(b)	-3.80	4.72	-4.22	$8.3 \times 10^{-16}$	$-0.58 \pm 0.10$	$3.02 \pm 0.16$	$-4.43 \pm 0.24$
H $\alpha$	PDS 37	X-shooter	-111.40	4.13	-115.53	$2.0 \times 10^{-13}$	$2.07 \pm 0.08$	$4.54 \pm 0.04$	$-2.87 \pm 0.22$
H $\alpha$	PDS 37	FORS2	-122.60	4.13	-126.73	$2.2 \times 10^{-13}$	$2.11 \pm 0.08$	$4.58 \pm 0.04$	$-2.83 \pm 0.22$
[OI] <sub>6300</sub>	PDS 37	X-shooter	-0.47	0.00	-0.47	$9.6 \times 10^{-16}$	$-0.25 \pm 0.08$	$4.51 \pm 0.36$	$-2.89 \pm 0.42$
[OI] <sub>6300</sub>	PDS 37	FORS2	-0.46	0.00	-0.46	$9.4 \times 10^{-16}$	$-0.26 \pm 0.08$	$4.50 \pm 0.35$	$-2.91 \pm 0.41$
Br $\gamma$	PDS 37	X-shooter	-8.50	4.64	-9.28	$1.2 \times 10^{-15}$	$-0.15 \pm 0.08$	$3.41 \pm 0.49$	$-4.00 \pm 0.53$

cess of energy seen across the Balmer jump region, and it has been observed in numerous CTTs (Gullbring et al. 2000; Herczeg & Hillenbrand 2008; Ingleby et al. 2013) and H AeBe stars (Garrison 1978; Muzerolle et al. 2004; Donehew & Brittain 2011; Mendigutía et al. 2011, 2014). The excess energy is often explained to be caused by magnetospheric accretion (MA), where disc material is funnelled via accretion columns on to the star where they shock the photosphere, with the final result of this being a hotspot of increased temperature that peaks in the UV (Calvet & Gullbring 1998). Therefore,  $\Delta D_B$  serves as a direct tracer of the accretion rate.

The method of measurement here follows Donehew & Brittain (2011), where the observed spectra and a model atmosphere of the star's temperature are normalised to 4000 Å, and then the spectra are adjusted by a reddening law until the slope of the SED

matches that of the model between 4000 and 4600 Å; this accounts for any reddening in the spectra, and has been shown to be reddening independent (Muzerolle et al. 2004; Donehew & Brittain 2011). Finally, the Balmer excess is measured by the equation:

$$\Delta D_B = 2.5 \log \left( \frac{F_* + F_{acc}}{F_*} \right) \quad (4)$$

where  $F_*$  is the flux of the photosphere at 3600 Å;  $F_{acc}$  is the flux produced due to accretion, at 3600 Å, such that  $F_* + F_{acc}$  is the observed flux. Fig. 8 shows the Balmer jump region of each object and the expected intrinsic photosphere, given by a KC model. The spectra is binned to 5 Å resolution in order to clearly see and measure the excess, and the region measured is from 3605 to 3665 Å to avoid the poor SNR region where the echelle orders crossover.  $\Delta D_B$  is measured to be  $0.17 \pm 0.06$  for PDS 27 and  $0.16 \pm 0.04$  for PDS

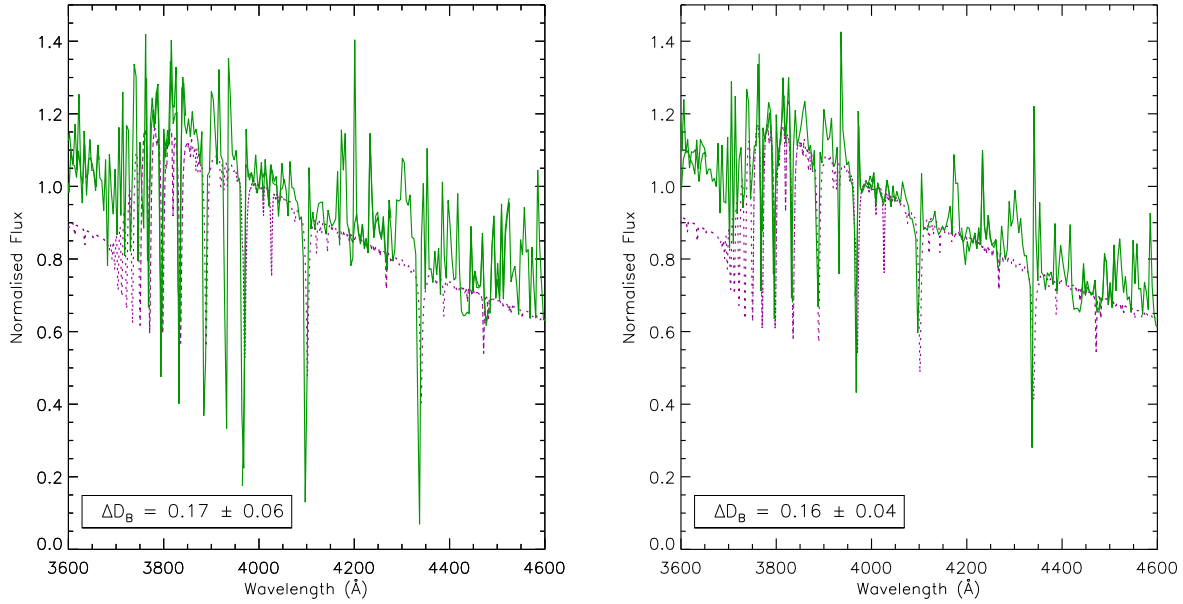


**Figure 8.** The Balmer jump region for PDS 27 (left) and PDS 37 (right). The targets are shown as the green solid line while the magenta dotted line is a KC model of 17500 K. The plot also highlights the extreme emission line nature of the two objects. The error in the Balmer excess displayed is solely the error due to the measurement between the two spectra.

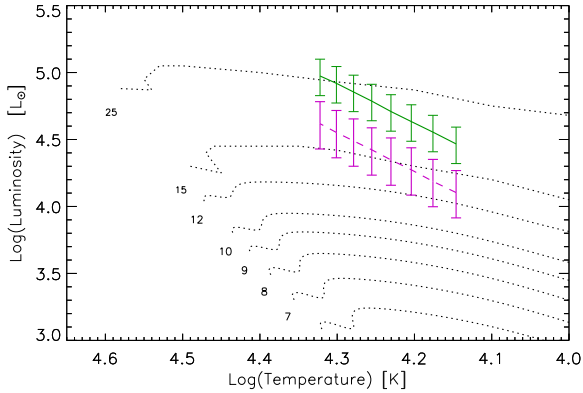


**Figure 7.** Shows the PMS tracks of Bernasconi & Maeder (1996) and Siess et al. (2000), along with the positions of PDS 27 in magenta dashed line and PDS 37 in green solid line. The dotted lines show where the objects lie for the determined temperature range, while the error bars show the allowed changes in luminosity given the errors in distance.

37. However, because of the temperature range adopted, the measured  $\Delta D_B$  can vary by more than this error (see Fig. 9). Therefore, we assign larger, more generous, errors to these measurements of 0.17 (+0.13, -0.16) for PDS 27 and 0.16 (+0.22, -0.15) for PDS 37.

As mentioned in Section 4.1.3, an upper limit was placed on the temperature of the stars by considering the observed size of the Balmer jump region. For the case of stars with an excess flux in this region, due to accretion, we can instead measure the Balmer excess, which is the amount

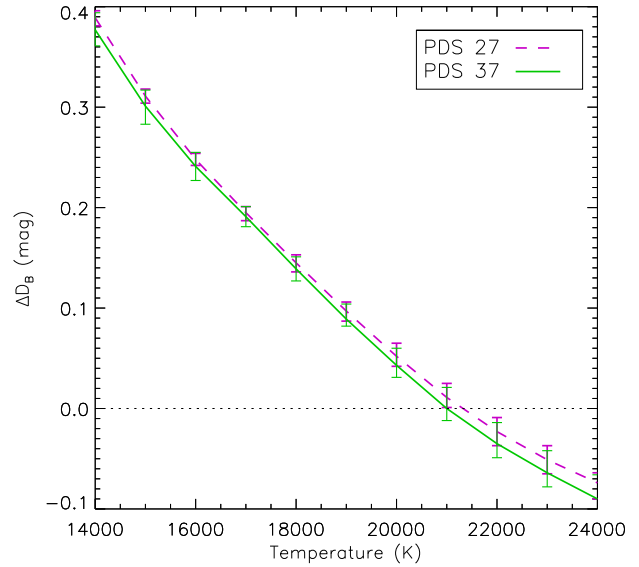


**Figure 9.** The measured Balmer excess changes for each star depending upon the adopted temperature. PDS 27 is shown in magenta dashed line, and PDS 37 in green solid line. For both stars, a zero in Balmer excess is achieved around 21000 K.

the Balmer jump is filled in by the excess flux. In Fig. 9 the observed Balmer excess for each star is shown for different temperatures (i.e. different Balmer jump sizes) to highlight

that there is a limit in temperature beyond which no excess can be observed.

The relationship between  $\Delta D_B$  and  $\dot{M}_{\text{acc}}$  depends upon the stellar parameters of the star, and a full description is given in Mendigutía et al. (2011). The basics are that the derivation of  $\dot{M}_{\text{acc}}$  from  $\Delta D_B$  is unique for each combination of stellar parameters, i.e. in a 20000 K star the same measured  $\Delta D_B$  will yield a much higher accretion rate than a 10000 K star because it requires a much higher accretion flux for the same visible  $\Delta D_B$ . Because of this, it also means that for hotter objects smaller  $\Delta D_B$  values are expected due to the sheer amount of accretion flux required to be noticeable above the photospheric level.

For the parameters determined in this work, the  $\log(\dot{M}_{\text{acc}})$  found are -3.96 (+0.76, -1.32) for PDS 27 and -3.56 (+0.60, -1.62) for PDS 37. Filling factors are also determined of  $f = 0.40$  (+0.55, -0.40) and 0.40 (0.54, -0.39), for PDS 27 and 37, respectively, when using a typical inward flux of accretion column energy of  $10^{12}$  erg/cm<sup>2</sup>/s (Mendigutía et al. 2011). These are large but acceptable filling factors.

#### 4.2.2 Accretion rates 2: line luminosity

For the second method, there are established relationships between accretion rate and emission line strength. This is because during the accretion process large amounts of energy are released which can excite the circumstellar environment. This excitation and excess of emission in CTTs can be explained by MA (Calvet & Gullbring 1998; Muzerolle, Calvet & Hartmann 1998). Well-established line strength relationships have been found for brown dwarfs (Natta et al. 2004, 2006; White & Basri 2003), CTTs (Muzerolle, Hartmann & Calvet 1998; Dahm 2008; Ingleby et al. 2013; Alcalá et al. 2014) and H AeBe stars (García López et al. 2006; Mendigutía et al. 2011). Since the two objects in this work are early-type Herbig stars, the relationships of Mendigutía et al. (2011) are adopted. However, it should be noted that these relationships may not hold for the targets in this work which are highly luminous compared to the stars from which the relationship was derived. This is an aspect we aim to test with the direct  $\Delta D_B$  derived accretion rate.

To obtain the line luminosities, a dereddened line flux is needed. This requires a line strength to be measured, which must be corrected for intrinsic line strength. The observed, intrinsic and corrected line strengths are given in Table 4. For the Br $\gamma$  line, it should be noted that the intrinsic correction must also take into account the IR excess in the  $K$  band. This is done following the steps in García López et al. (2006). The flux density is then calculated from an interpolation between the two closest photometric points; with the exception of the Br $\gamma$  line for which no interpolation is made, instead the value of the  $K$ -band magnitude is used. The photometry is dereddened by the  $A_V$  values found in Section 4.1.4 prior to this step. The line flux is obtained by multiplication of the interpolated flux density and the line strength, and the line luminosity is then achieved by multiplying the line flux by  $4\pi D^2$ .

Once the line luminosity is established, the accretion luminosity for each line is extracted via the relationships of Mendigutía et al. (2011) which take the form of  $\log(L_{\text{acc}}) =$

$A + B \log(L_{\text{line}})$ , where  $A$  and  $B$  are constants specific to each line. Finally, the accretion rate is calculated via the equation:  $\dot{M}_{\text{acc}} = L_{\text{acc}} R_*/GM_*$ , where  $G$  is the gravitational constant and  $\dot{M}_{\text{acc}}$  is the accretion rate. Table 4 gives details of the values used to derive the accretion rates. The accretion rates derived from the H $\alpha$ , [O I] and Br $\gamma$  lines are in the range of  $\dot{M}_{\text{acc}} \sim 10^{-3}$ – $10^{-4.5} M_{\odot}/\text{yr}$ .

## 5 DISCUSSION

We have presented a spectroscopic and spectropolarimetric study of two early-type Herbig stars, and found that the spectra of both objects are remarkably similar, strongly suggesting that both are in the same evolutionary phase. The spectra are dominated by strong emission lines, and do not reveal any photospheric absorption lines. Indeed, the only lines that are fully in absorption are the interstellar DIB lines.

The picture that emerges is that both objects undergo strong winds as attested by the clear, and numerous, P Cygni profiles observed. P Cygni absorption extends in both stars to hundreds of km s<sup>-1</sup>. The He I line at 10830 Å is the only helium line seen as a P Cygni profile. The remaining He I lines at 5875, 6678 and 7065 Å are present only in absorption (see Fig. 3). These lines are broader than the expected intrinsic lines from the photosphere. If they originate from the wind, they must probe the very hot inner wind.

### 5.1 Circumstellar geometry

The majority of the observed Fe II lines are double peaked in PDS 37, while they are single peaked in PDS 27 (see Section 3.1). This suggests that PDS 37 has an inclined disc that we are viewing close to edge-on. This interpretation is supported by a high inclination angle being reported by Ilee et al. (2013), based on first overtone CO emission. In addition, the continuum polarisation shows a change in position angle with wavelength. The observed polarisation must have an intrinsic component as normally the interstellar polarisation angle is constant with wavelength. This change is stronger in PDS 37 than PDS 27 as illustrated in Fig. 4. Further information on the geometry of the circumstellar environment can be achieved by performing spectropolarimetry across the lines.

Spectropolarimetry is very effective in revealing asymmetries in the scattering material. This technique is based on the concept that free electrons very close to the stars, where the density of free electrons is high due to hydrogen ionisation, scatter the continuum radiation from the stellar photosphere and polarise it. The electron scattering region is of the order of a few stellar radii (Cassinelli et al. 1987). In the case of a face-on disc, or if surrounding material is spherically symmetric, no net polarisation can be detected, while in the case of inclined flattened structures a net polarisation can be observed. The emission lines are less polarised than the continuum radiation because they face fewer electrons than the continuum and the ionised region is larger than the electron scattering region. Clarke & McLean (1974) and Poeckert & Marlborough (1976) first used spectropolarimetry in a study of Be stars, which allowed them to infer that these stars are surrounded by discs.



A change in polarisation across the absorptive component of the emission line can not be explained by the above concept, and is often suggested to be the result of the McLean effect. In brief, the absorption takes the direct, unscattered, light from the star away from the beam; however, the flux does not necessarily reach zero. Some of the light emitted in other directions can be scattered into our line of sight by free electrons, provided the electrons are in a non-spherical distribution. Therefore, the observed light in the absorption region will be more polarised than the continuum (McLean 1979). There are many objects reported as having a McLean effect; see for example Vink et al. (2005)

Both PDS 27 and PDS 37 show a strong McLean-type effect across the absorptive component of  $H\alpha$  (see Fig. 5) and the change is as broad as the absorption. This indicates the presence of intrinsic polarisation which in turn implies that the ionised material around the star is asymmetrically distributed. The strength of the line effect in  $H\alpha$  is of the order of 1% in PDS 27 and 1.6% in PDS 37. This supports the ideas that PDS 37 has a more inclined disc than PDS 27, as we expect more intrinsic polarisation in a more inclined disc. The slope of the loop from the continuum to the line in the  $(Q, U)$  diagram represents the intrinsic polarisation for the continuum polarisation (see Fig. 5). The intrinsic continuum polarisation angle represents the electron scattering angle in the circumstellar medium. We determine an intrinsic polarisation angle of  $\sim 77^\circ$  for PDS 27 and  $\sim 56^\circ$  for PDS 37. The angle has been measured from the continuum to the line in the  $(Q, U)$  diagram in Fig. 5 [see the discussion in Wheelwright et al. (2011)].

We would expect a similar line effect in  $H\beta$  as in  $H\alpha$ , since it arises from approximately the same volume. However, we do not see any changes across the line profile, neither in absorption nor in the emission (see Fig. 5). A point noteworthy is that the absorption component in  $H\beta$  is deeper than that of  $H\alpha$ , which is not intrinsically expected as the latter has a greater optical depth than the former.

In the present cases, we are able to explain this relatively straightforwardly, by using the information that the strong emission from  $H\alpha$  is scattered into our line of sight, filling in its P Cygni absorption component with scattered, polarised emission. In contrast,  $H\beta$  is a much weaker emission line, and therefore far fewer photons are available to be scattered into the line of sight compared to  $H\alpha$ . As a consequence, weaker, if any, changes in polarisation across the P Cygni absorption would be predicted in this model. This explains a non-detection of the line effect across the absorption component in  $H\beta$ . This argument can also explain why the  $H\alpha$  line effect in PDS 37 is more obvious than the one in PDS 27, as the latter line has deeper absorption components. For all of the other emission lines covered by the FORS2 spectropolarimetry of both stars, we do not detect a line effect.

To summarise, we do not see a line effect across the  $H\beta$  line as the majority of the photons in the absorption component are unscattered light. The observed He I emission lines are weak and they do not show any line effect, and the line effect across the Ca II triplet in PDS 37 is not compelling. However, from the characteristics of the observed spectral lines, along with the continuum polarisation and the line spectropolarimetry across the  $H\alpha$  line, we can confirm that these two objects have an asymmetric circumstellar environ-

ment. We identify this to be a circumstellar disc, whose size is at least of the order of several stellar radii.

## 5.2 Stellar properties

Based on their position in the HR diagram, we can infer that both of the targets are young objects with an active circumstellar environment. This is evidenced by high accretion rates of  $(\dot{M}_{\text{acc}}) = 10^{-3}\text{--}10^{-4.5} \text{ M}_{\odot}\text{yr}^{-1}$ ; strong winds, with P Cygni absorption of around 90 and 80% of continuum level for PDS 27 and PDS 37, respectively, in  $H\beta$ , and also maximum respective velocities of  $\sim 700$  and  $\sim 400 \text{ km s}^{-1}$  measured in the  $H\alpha$  line; and variability in line strengths and velocities seen in both the hydrogen and the He I lines. In particular, PDS 27 has shown unusual variability in the He I lines where the velocity of the line centre and the line strength change dramatically between epochs. This type of variability in line strength has been observed previously in other objects by Kučerová et al. (2013), but an origin of the varying line strength cannot be reached with only three epochs of data. PDS 27 also shows variability in the observed  $V_{\text{LSR}}$  between the X-shooter and FORS2 spectra. This could be due to the presence of a secondary companion. However, with only three epochs of data, we cannot establish conclusively the binary nature of PDS 27; additional data are required to determine the frequency and magnitude of the velocity variations. Unlike PDS 27, PDS 37 did not show any variability in the observed  $V_{\text{LSR}}$  between X-shooter and FORS2 spectra.

Their young age is further supported by their large radii and low surface gravities. These properties are typical of very young objects where their puffed-up envelope is still undergoing contraction and will shrink as it progresses towards the main-sequence (Davies et al. 2010). The accretion rates obtained from the  $H\alpha$  and [O I] 6300 Å are found to be the same across all epochs, within the errors, for both PDS 27 and PDS 37. These two lines also show that PDS 37 has an accretion rate  $\sim 0.6$  dex greater than PDS 27, which is comparable to the difference seen between the accretion rates derived from the Balmer excess of  $\sim 0.4$ ; both are within the errors. The Br $\gamma$  line does not follow the same trends as it shows a decrease in accretion rate, in both objects, over both the other two lines and the Balmer excess measurement (see Table 4 for all of the emission line derived accretion rates).

The accretion rates derived using the Br $\gamma$  line are higher than any other reported accretion rates in HBe stars, which also use the Br $\gamma$  line, by  $\sim 1\text{--}3$  orders of magnitude (García Lopez et al. 2006; Donehew & Brittain 2011). The Balmer excess method results in  $\log(\dot{M}_{\text{acc}}) = -3.96 (+0.76, -1.32)$  for PDS 27 and  $-3.56 (+0.60, -1.62)$  for PDS 37. These values agree with the respective accretion rates derived from all of the lines analysed. The Br $\gamma$  line in both objects shows a difference of an order of magnitude less in accretion rate between the other lines. A possible breakdown in the relationship between line luminosity and accretion luminosity has been suggested by Donehew & Brittain (2011), where the luminosity increases towards the early-type HAeBe star regime. However, the two stars presented in this work still follow this relationship. We cannot conclude with just these two objects whether the relationship holds or not, and such is beyond the scope of this paper. Instead, PDS 27 and PDS



37 will form part of an upcoming paper exploring these relationships in a larger sample (Fairlamb et al., in preparation).

## 6 CONCLUSIONS

This work presents new data on two previously poorly studied H AeBe candidate stars. By combining X-shooter spectroscopy and FORS2 spectropolarimetry, our understanding of properties in the circumstellar environments and the stellar parameters of the stars themselves has improved. The main findings in this work are as follows:

- The targets are both very hot  $17500 \pm 3500$  K with a spectral type of around B2. When combined with their high luminosities, of  $\log(L_*/L_\odot) \sim 4.5$ , they are placed in a secluded area on the HR diagram where very young objects lie. They are swollen objects with large radii,  $17.0 \pm 4.0$  and  $25.8 \pm 5.0 R_\odot$ , and large masses,  $15.3 (+5.4, -4.4)$  and  $21.1 (+11.0, -5.3) M_\odot$ , for PDS 27 and 37 respectively. Their young nature is supported by the high accretion rates calculated here, which are among the highest measured in H AeBe stars to date,  $\dot{M}_{\text{acc}} \sim 10^{-3} - 10^{-4.5} M_\odot \text{yr}^{-1}$ .

- Spectropolarimetric line effects are detected in the H $\alpha$  line for both objects. This polarisation property is explained by the McLean effect; line photons are scattered into the line of sight, increasing the polarisation across the P Cygni absorption. The spectropolarimetry indicates that the circumstellar environment is of a flattened structure, likely a disc.

- No line effects are seen across lines other than H $\alpha$ . This is consistent with the notion that the spectropolarimetric behaviour in both cases is due to the McLean effect. The effect requires a strong emission line filling in absorption and a line with great optical depth so that the scattered photons will dominate the polarisation. It appears that in the cases studied here, only H $\alpha$  fulfils both requirements.

- Line variability is seen in both objects, which we ascribe to an active circumstellar environment. Extreme line variability of the He I species is seen in PDS 27. In addition, PDS 27 also shows a variability in the observed  $V_{\text{LSR}}$  between X-shooter and FORS2; this could be due to the fact that the system is binary.

Finally, we have presented two young PMS stars, whose spectral classification as early B-type is consistent with them belonging to the group of H AeBe stars. Their masses and locations in the HR diagram indicate that they will continue to evolve to become O-type stars. As they are optically bright, these stars provide important test beds to study the formation of the most massive stars.

## ACKNOWLEDGEMENTS

The authors would like to thank the ESO staff for carrying out the observations in service mode. Jorick Vink is thanked for helpful discussions. KMA is supported by the Human Capacity Development Program (HCDP) in Kurdistan-Iraq. JRF is supported by the UK Science and Technology Facilities Council (STFC).

## REFERENCES

- Alcalá J. M., Natta A., Manara C. F., Spezzi L., Stelzer B., Frasca A., Biazio K., Covino E., Randich S., Rigliaco E., Testi L., Comerón F., Cupani G., D’Elia V., 2014, *A&A*, 561, A2
- Beristain G., Edwards S., Kwan J., 2001, *ApJ*, 551, 1037
- Bernasconi P. A., Maeder A., 1996, *A&A*, 307, 829
- Calvet N., Gullbring E., 1998, *ApJ*, 509, 802
- Cassinelli J. P., Nordsieck K. H., Murison M. A., 1987, *ApJ*, 317, 290
- Castelli F., Kurucz R. L., 2004, *ArXiv Astrophysics e-prints*, astro-ph/0405087
- Chlewicki G., van der Zwet G. P., van Ijzendoorn L. J., Greenberg J. M., Alvarez P. P., 1986, *ApJ*, 305, 455
- Clarke D., McLean I. S., 1974, *MNRAS*, 167, 27P
- Dahm S. E., 2008, *ApJ*, 136, 521
- Davies B., Lumsden S. L., Hoare M. G., Oudmaijer R. D., de Wit W.-J., 2010, *MNRAS*, 402, 1504
- Delbouille L., Roland G., Neven L., 1973, *Atlas photometrique du spectre solaire de  $\lambda$  3000 a  $\lambda$  10000*. Institut d’Astrophysique, Universite de Liege, Liege
- Donehew B., Brittain S., 2011, *ApJ*, 141, 46
- Fairlamb J. R., Oudmaijer R. D., Mendigutia I., Ilee J. D., van den Ancker M. E., 2015, *MNRAS*, in press
- Garcia Lopez R., Natta A., Testi L., Habart E., 2006, *A&A*, 459, 837
- Garrison Jr. L. M., 1978, *ApJ*, 224, 535
- Gullbring E., Calvet N., Muzerolle J., Hartmann L., 2000, *ApJ*, 544, 927
- Hamann F., Persson S. E., 1992, *ApJS*, 82, 285
- Herbig G. H., 1960, *ApJS*, 4, 337
- Herczeg G. J., Hillenbrand L. A., 2008, *ApJ*, 681, 594
- Ilee J. D., Wheelwright H. E., Oudmaijer R. D., de Wit W. J., Maud L. T., Hoare M. G., Lumsden S. L., Moore T. J. T., Urquhart J. S., Mottram J. C., 2013, *MNRAS*, 429, 2960
- Ingleby L., Calvet N., Herczeg G., Blaty A., Walter F., Ardila D., Alexander R., Edwards S., Espaillet C., Gregory S. G., Hillenbrand L., Brown A., 2013, *ApJ*, 767, 112
- Jenniskens P., Desert F.-X., 1994, *A&AS*, 106, 39
- Kurosawa R., Romanova M. M., Harries T. J., 2011, *MNRAS*, 416, 2623
- Kurucz R. L., 1993, *SYNTHES spectrum synthesis programs and line data*
- Kučerová B., Korčáková D., Polster J., Wolf M., Votruba V., Kubát J., Škoda P., Šlechta M., Krížek M., 2013, *A&A*, 554, A143
- Lumsden S. L., Hoare M. G., Urquhart J. S., Oudmaijer R. D., Davies B., Mottram J. C., Cooper H. D. B., Moore T. J. T., 2013, *ApJS*, 208, 11
- McLean I. S., 1979, *MNRAS*, 186, 265
- Mendigutia I., Calvet N., Montesinos B., Mora A., Muzerolle J., Eiroa C., Oudmaijer R. D., Merín B., 2011, *A&A*, 535, A99
- Mendigutia I., Fairlamb J., Montesinos B., Oudmaijer R. D., Najita J. R., Brittain S. D., van den Ancker M. E., 2014, *ApJ*, 790, 21
- Modigliani A., Goldoni P., Royer F., Haigron R., Guglielmi L., François P., Horrobin M., Bristow P., Vernet J., Moehler S., Kerber F., Ballester P., Mason E., Christensen

- L., 2010, in Society of Photo-Optical Instrumentation Engineers (SPIE) Conference Series Vol. 7737 of Society of Photo-Optical Instrumentation Engineers (SPIE) Conference Series, The X-shooter pipeline
- Muzerolle J., Calvet N., Hartmann L., 1998, *ApJ*, 492, 743
- Muzerolle J., D'Alessio P., Calvet N., Hartmann L., 2004, *ApJ*, 617, 406
- Muzerolle J., Hartmann L., Calvet N., 1998, *ApJ*, 116, 2965
- Natta A., Testi L., Muzerolle J., Randich S., Comerón F., Persi P., 2004, *A&A*, 424, 603
- Natta A., Testi L., Randich S., 2006, *A&A*, 452, 245
- Ochsendorf B. B., Ellerbroek L. E., Chini R., Hartoog O. E., Hoffmeister V., Waters L. B. F. M., Kaper L., 2011, *A&A*, 536, L1
- Oudmaijer R. D., Busfield G., Drew J. E., 1997, *MNRAS*, 291, 797
- Oudmaijer R. D., Drew J. E., 1999, *MNRAS*, 305, 166
- Oudmaijer R. D., van den Ancker M. E., Baines D., Caselli P., Drew J. E., Hoare M. G., Lumsden S. L., Montesinos B., Sim S., Vink J. S., Wheelwright H. E., de Wit W. J., 2011, *Astronomische Nachrichten*, 332, 238
- Poeckert R., Marlborough J. M., 1976, *ApJ*, 206, 182
- Reid M. J., Menten K. M., Brunthaler A., Zheng X. W., Moscadelli L., Xu Y., 2009, *ApJ*, 693, 397
- Rodrigues C. V., Sartori M. J., Gregorio-Hetem J., Magalhães A. M., 2009, *ApJ*, 698, 2031
- Serkowski K., Mathewson D. S., Ford V. L., 1975, *ApJ*, 196, 261
- Siess L., Dufour E., Forestini M., 2000, *A&A*, 358, 593
- Suárez O., García-Lario P., Machado A., Manteiga M., Ulla A., Pottasch S. R., 2006, *A&A*, 458, 173
- Testi L., Palla F., Natta A., 1999, *A&A*, 342, 515
- The P. S., de Winter D., Perez M. R., 1994, *A&AS*, 104, 315
- Urquhart J. S., Busfield A. L., Hoare M. G., Lumsden S. L., Oudmaijer R. D., Moore T. J. T., Gibb A. G., Purcell C. R., Burton M. G., Marechal L. J. L., 2007, *A&A*, 474, 891
- Urquhart J. S., Morgan L. K., Figura C. C., Moore T. J. T., Lumsden S. L., Hoare M. G., Oudmaijer R. D., Mottram J. C., Davies B., Dunham M. K., 2011, *MNRAS*, 418, 1689
- Vernet J., Dekker H., D'Odorico S., Kaper et al., 2011, *A&A*, 536, A105
- Vieira R. G., Gregorio-Hetem J., Hetem A., Stasińska G., Szczerba R., 2011, *A&A*, 526, A24
- Vieira S. L. A., Corradi W. J. B., Alencar S. H. P., Mendes L. T. S., Torres C. A. O., Quast G. R., Guimarães M. M., da Silva L., 2003, *ApJ*, 126, 2971
- Vink J. S., Drew J. E., Harries T. J., Oudmaijer R. D., 2002, *MNRAS*, 337, 356
- Vink J. S., Drew J. E., Harries T. J., Oudmaijer R. D., Unruh Y., 2005, *MNRAS*, 359, 1049
- Waters L. B. F. M., Waelkens C., 1998, *ARA&A*, 36, 233
- Wheelwright H. E., Vink J. S., Oudmaijer R. D., Drew J. E., 2011, *A&A*, 532, A28
- White R. J., Basri G., 2003, *ApJ*, 582, 1109
- Zinnecker H., Yorke H. W., 2007, *ARA&A*, 45, 481